Power Electronics Research and Applications Transactions
https://www.sciltp.com/journals/perat

*Article*

# Multi-Condition PSO-FOPI Current-Sharing Control for Parallel LLC Resonant Converters under Parameter Deviations

Shicheng Yang [1], Liangzong He [1,*] and Jian Ye [2,*]

[1] School of Aerospace Engineering, Xiamen University, Xiamen 361102, China
[2] School of Vehicles and Intelligent Transportation, Fuyao University of Science and Technology, Fuzhou 350109, China
* Correspondence: hlz190213@163.com (L.H.); jianyee@fyust.org.cn (J.Y.)

**How To Cite:** Yang, S.; He, L.; Ye, J. Multi-Condition PSO-FOPI Current-Sharing Control for Parallel LLC Resonant Converters under Parameter Deviations. *Power Electronics Research and Applications Transactions* **2026**. https://doi.org/10.53941/perat.2026.100007

Received: 8 August 2026
Revised: 7 September 2026
Accepted: 9 September 2026
Published: 21 September 2026

**Abstract:** Parallel LLC resonant converters are suitable for low-voltage and high-current applications. However, deviations in the resonant inductor, resonant capacitor, and magnetizing inductor cause gain differences among phases, resulting in output-current imbalance. To address the difficulty of achieving satisfactory multi-condition dynamic performance with a dual-loop controller under unknown resonant-parameter deviations, this paper proposes a multi-condition particle swarm optimization fractional-order proportional-integral (PSO-FOPI) current-sharing control method. The proposed method adopts a common-mode/differential-mode frequency dual-loop structure, in which common output-voltage regulation and interphase current-sharing regulation are mapped to the common-mode and differential-mode frequencies, respectively. Meanwhile, the worst-case time-domain performance over typical parameter-deviation conditions is used as the fitness function, and particle swarm optimization (PSO) is employed to offline tune the dual-loop FOPI controller parameters. Simulation results show that, under six typical parameter-deviation conditions and within a ±15% Monte Carlo random parameter-deviation range, the controller maintains favorable voltage and current-sharing dynamic performance. Hardware experiments further verify the practical operating feasibility of the proposed control method.

**Keywords:** parallel LLC; current-sharing control; parameter deviation; FOPI; PSO

## 1. Introduction

In recent years, with the development of data centers, electric vehicles, 5G communication, DC microgrids, and renewable-energy systems, medium- and high-power isolated DC-DC converters have been required to provide higher efficiency, higher power density, and higher reliability. LLC resonant converters feature a simple structure, a wide soft-switching range, high efficiency, and high power density, and have therefore been widely used in consumer electronics, data centers, electric vehicles, and aerospace applications [1]. Meanwhile, solid-state transformers (SST), as an important power-electronic transformer technology for smart grids, generally require high-frequency isolated DC-DC stages for voltage conversion, power transfer, and modular interconnection [2]. LLC resonant DC-DC converters can also serve as high-frequency isolated conversion units in SST systems [3].

For low-voltage high-current applications or higher power levels, a single LLC module is limited by device current stress, magnetic-component volume, and thermal design. Therefore, multiphase parallel LLC structures are an important approach for increasing output-current capability and improving system modularity. However, in input-parallel output-parallel structures, current distribution among phases is easily affected by resonant-tank parameter deviations. When the resonant-tank components of different phases suffer from manufacturing tolerances, temperature drift, or aging differences, the resonant frequencies and voltage-gain curves of the phases shift. Under the constraint of a common output voltage, such shifts cause output-current imbalance, unequal device stress, and reduced system reliability [4,5]. Even small resonant-parameter deviations may cause significant current imbalance [4].

Existing current-sharing methods for multiphase LLC converters can generally be classified into passive and active current-sharing methods. Passive current-sharing methods achieve natural current sharing mainly by changing the topology, magnetic connection, or impedance-matching relationship. Examples include secondary-winding reconstruction, common-inductor/common-capacitor structures, coupled resonant tanks, and natural phase-shedding structures [6–9]. These methods usually do not require complex current sampling or closed-loop control, but their current-sharing performance depends on specific topologies, magnetic structures, or impedance-matching conditions. Some active current-sharing methods introduce additional controllable components or auxiliary regulation units for parameter compensation, such as switched capacitors, variable resonant tanks, resonant-capacitor energy regulation, differentiated gain regulation, and fractional-order auxiliary current-sharing units [10–14]. These methods have strong parameter-compensation capability but generally increase the number of additional components, control circuits, or sensing requirements.

By contrast, active current-sharing methods based on the original bridge-leg drive signals offer a more direct implementation. These methods usually sample information such as the output voltage, phase currents, or total current, and regulate the switching frequency, phase-shift angle, or duty cycle to modify the power distribution among phases and suppress the current imbalance caused by parameter deviations [15–18]. Further studies have introduced modified disturbance rejection, combined variable-frequency and phase-shift control, model predictive control (MPC), or fewer-sensor iterative optimization to improve the robustness of parallel LLC converters under parameter disturbances and load variations [19–24]. These methods can achieve good steady-state current-sharing performance and stable dynamic responses during load switching. Nevertheless, under unknown resonant-parameter deviations, how to systematically tune the controller parameters and whether good stability and dynamic performance can be maintained over a certain parameter-deviation range remain open issues. In addition, when resonant-parameter deviations have already caused undesired output-current imbalance between the two phases, the transient process from an unbalanced state to a balanced state can more directly reflect the regulation capability of the current-sharing controller.

To address these issues, this paper adopts a common-mode/differential-mode frequency dual-loop control structure, in which common output-voltage regulation is mapped to the common-mode frequency and two-phase current-sharing regulation is mapped to the differential-mode frequency. The fractional-order proportional-integral (FOPI) controller extends the conventional proportional-integral (PI) controller by introducing an additional degree of freedom through the fractional integration order. Because the dual-loop controller parameters simultaneously affect the voltage settling time, current-sharing settling time, overshoot, and load-disturbance recovery performance, manual tuning is inefficient and may yield parameters applicable only to specific conditions. Particle swarm optimization (PSO) is gradient-free, structurally simple, and suitable for nonlinear multi-parameter optimization; it has been used for controller-parameter tuning in power electronic converters [25]. The remainder of this paper is organized as follows. Section 2 analyzes the current-sharing mechanism of the two-phase parallel LLC resonant converter and establishes the common-mode/differential-mode dual-loop FOPI control structure. Section 3 formulates the multi-condition PSO-FOPI parameter-tuning method for resonant-parameter deviations, including the parameter-deviation condition set, fitness function, and optimization process. Section 4 verifies the dynamic performance and operating stability of the proposed method under unknown parameter deviations through typical parameter-deviation simulations, Monte Carlo random parameter-deviation simulations, and hardware experiments. Sections 5 and 6 provide the discussion and conclusions, respectively.

## 2. Parameter Deviation and Dual-Loop FOPI Control Structure for Parallel LLC Converters

### *2.1. Two-Phase Parallel LLC Structure and Current-Sharing Issue*

This paper focuses on a two-phase half-bridge LLC resonant converter with an input-parallel output-parallel structure, as shown in Figure 1. The system consists of two structurally identical half-bridge LLC modules connected in parallel. Each module includes a half-bridge inverter, a resonant inductor, a resonant capacitor, a magnetizing inductor, a high-frequency transformer, and an output rectifier-filter circuit. The input terminals of the two LLC modules are connected to the same DC bus, while their output terminals are connected in parallel to a common output capacitor and load. This structure increases the output-current capability through module paralleling and reduces the current and thermal stresses of a single module, making it suitable for low-voltage high-current and medium- to high-power DC conversion applications.

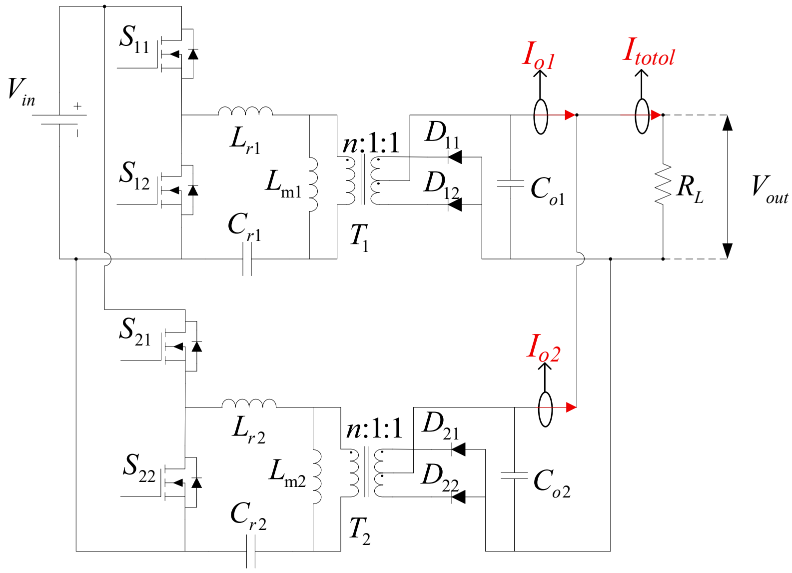


**Figure 1.** Topology of the two-phase parallel-connected half-bridge LLC resonant converter.

Under ideal conditions, the two LLC phases have identical resonant-tank parameters and therefore have identical voltage gains and power-transfer capabilities at the same switching frequency, so the output currents can be naturally shared. In practical systems, however, the resonant inductor, resonant capacitor, and magnetizing inductor are inevitably affected by manufacturing tolerances, temperature drift, magnetic-component nonlinearity, and aging. These factors shift the resonant frequency and gain curve of each phase. Even small resonant-tank parameter differences in a multiphase LLC converter can cause significant output-current imbalance.

For an output-parallel structure, the secondary sides of the two phases are connected to the same output capacitor and load, so the output voltages of the two phases are clamped to the same common-bus voltage. When resonant-parameter deviations cause a difference in the voltage gains of the two phases, their power-transfer capabilities at the same operating condition become different. The phase with a higher gain tends to deliver more current and power to the common bus, whereas the phase with a lower gain exhibits reduced power-transfer capability and consequently supplies less output current. In severe cases, the low-gain phase may provide very little output current, while the high-gain phase carries most of the load current. Therefore, parameter deviations not only cause steady-state current imbalance between the two phases but also aggravate the loss and thermal stress of a single module. Accordingly, the control objectives of the parallel LLC converter include not only maintaining a stable common output voltage but also suppressing the output-current difference between the two phases under parameter deviations, so that the modules share the load power more evenly. In this paper, "parameter deviation" refers to the deviation of resonant-tank parameters, including $L_r$, $C_r$, and $L_m$, from their nominal values. When the deviations of the two phases are different, they cause interphase gain differences and undesired output-current imbalance in the equal-rated parallel-connected modules.

## *2.2. Common-Mode/Differential-Mode Frequency Dual-Loop Control Structure*

To separately describe output-voltage regulation and two-phase power distribution, this paper adopts a common-mode/differential-mode frequency control structure, as shown in Figure 2. The common-mode frequency regulates the overall energy-transfer capability of the two LLC phases and primarily determines the common output voltage, whereas the differential-mode frequency regulates the energy distribution between the two phases and primarily determines the output-current difference. The actual switching frequencies of the two phases are synthesized from the common-mode frequency and the differential-mode frequency: $f_1 = f_{base} + f_{diff}$ , $f_2 = f_{base} - f_{diff}$ .When the common-mode frequency changes, the two phase frequencies vary in the same direction and the total output power of the system changes accordingly. When the differential-mode frequency changes, the two phase frequencies vary in opposite directions and the output-current distribution between the phases changes accordingly.

The controller samples the common output voltage and the two phase output currents. Because the LLC output current and voltage contain high-frequency AC components caused by the switching frequency and rectification, the sampled signals are first processed by first-order inertial filters to extract the low-frequency averaged quantities used for control. The inertial filter is expressed as

$$G_f(s) = \frac{1}{T_f s + 1} \tag{1}$$

The voltage-loop error is defined as the output-voltage deviation normalized by the reference voltage, and the current-sharing-loop error is defined as the two-phase output-current difference normalized by the total current:

$$\begin{aligned} e_v &= \frac{V_{ref} - V_o}{V_{ref}} \\ e_i &= \frac{I_{o1} - I_{o2}}{I_{o1} + I_{o2}} \end{aligned} \tag{2}$$

Here, $V_{ref}$ is the output-voltage reference and $T_f$ is the inertial-filter time constant. In this work, $T_f$ is set to $10^{-5}$ s for both voltage and current sampling. The voltage error is fed into the voltage-loop FOPI controller, which outputs the common-mode frequency correction, while the current-sharing error is fed into the current-sharing-loop FOPI controller, which outputs the differential-mode frequency correction. The two actual switching frequencies are then obtained by the frequency-synthesis module and sent to the pulse-width modulation (PWM) generator to drive the two LLC phases.

The voltage loop is mainly responsible for stabilizing the common bus voltage, whereas the current-sharing loop is mainly responsible for distributing the two phase currents. It should be noted that LLC converters have nonlinear frequency-gain characteristics, and the final frequencies of both phases influence the resonant-tank power transfer. Therefore, the voltage loop and current-sharing loop are not strictly decoupled: differential-mode regulation may disturb the output voltage, while common-mode regulation may also affect the two-phase current difference. For this reason, the subsequent controller tuning in this paper does not rely only on the nominal condition but evaluates the comprehensive performance of the dual-loop controller through multi-condition closed-loop simulations.

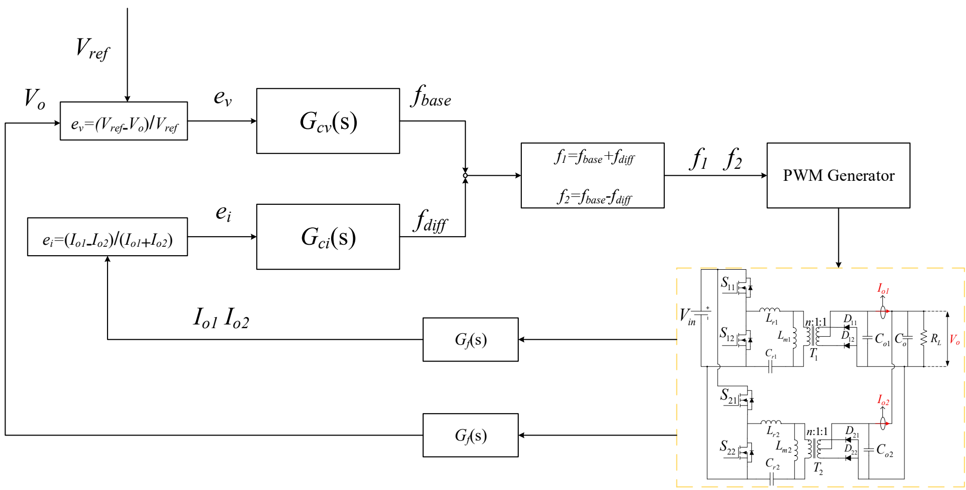


**Figure 2.** Common-mode/differential-mode frequency dual-loop FOPI control structure.

## *2.3. Engineering Implementation of the FOPI Controller*

In the dual-loop structure described above, both the voltage loop and the current-sharing loop adopt FOPI controllers. Compared with a conventional PI controller, a FOPI controller introduces a fractional-order degree of freedom beyond the proportional and integral gains, thereby providing extra flexibility for adjusting the magnitude- and phase-frequency characteristics of the controller. Following the original controller definition used in this paper, the FOPI controller is described as an integrator of order $1+\lambda$:

$$G_c(s) = K_p + \frac{K_i}{s^{1+\lambda}} \tag{3}$$

where $K_p$ is the proportional gain, $K_i$ is the integral gain, and $\lambda$ is the additional fractional order. When $\lambda = 0$, the controller degenerates into a conventional PI controller. To facilitate digital implementation, the fractional integration term is split into an integer-order integral part and a residual fractional-order part:

$s^{-(1+\lambda)} = s^{-1} \cdot s^{-\lambda}$. Thus, the controller can be interpreted as follows: the error signal first passes through a residual fractional-order integration process and then enters a conventional integer-order integrator. The integer-order integrator retains low-frequency error accumulation to reduce steady-state error, whereas the fractional-order part modifies the dynamic characteristics of the controller through finite memory, providing additional freedom for shaping the closed-loop response.

Fractional-order operators have infinite memory and cannot be directly implemented in digital controllers. This paper adopts the Grünwald-Letnikov (GL) discrete approximation and truncates it with a finite-length sliding window [26]. Let the control period be $T_s$, the truncation length be $L$ (set to 30 in this paper), and the error signal be $e(k)$. The intermediate variable after residual fractional-order integration can be written as:

$$e_f(k) = T_s^{\lambda}\sum_{j=0}^{L-1} w_j e(k-j) \tag{4}$$

where $w_j$ denotes the GL expansion weight. The weights can be calculated offline through the recurrence relationship:

$$\begin{gathered} w_0 = 1 \\ w_j = w_{j-1}\frac{j-1+\lambda}{j}, j = 1,2,\cdots,L-1 \end{gathered} \tag{5}$$

To avoid large differences in the DC gain of the weights under different fractional orders, the GL weights are normalized:

$$\hat{w}_j = \frac{w_j}{\sum_{m=0}^{L-1} w_m} \tag{6}$$

After normalization, the fractional intermediate variable is:

$$e_f(k) = \sum_{j=0}^{L-1} \hat{w}_j e(k-j) \tag{7}$$

After $e_f(k)$ is obtained, the integer-order integrator is implemented using backward Euler discretization:

$$I(k) = I(k-1) + K_i T_s e_f(k) \tag{8}$$

The final controller output is:

$$u(k) = K_p e(k) + I(k) \tag{9}$$

In the voltage loop, $u(k)$ corresponds to the common-mode frequency correction, whereas it represents the differential-mode frequency correction in the current-sharing loop, which satisfies

$$\begin{aligned} \Delta f_{base}(k) &= K_{pv} e_v(k) + I_v(k) \\ \Delta f_{diff}(k) &= K_{pi} e_i(k) + I_i(k) \end{aligned} \tag{10}$$

The actual common-mode and differential-mode frequencies are then obtained by combining the initial frequency and limiting links. In engineering implementation, the GL weights can be precomputed and stored for a given $\lambda$ and truncation length $L$. During controller operation, only a finite-length multiply-accumulate operation and one integer-order integral update are required. The finite-length GL truncation is adopted to retain the historical memory characteristic of the fractional-order operator while reducing the storage and computational burden on the digital signal processor (DSP) or digital control platform.

Because the voltage loop and current-sharing loop have different control objectives, their FOPI parameters must be tuned separately. The voltage loop mainly affects the output-voltage recovery process; overly large parameters may cause oscillation of the common bus voltage. The current-sharing loop mainly affects the distribution of the two phase currents; overly small parameters slow down current-sharing, whereas overly large parameters may lead to excessive phase-frequency separation and alternating current oscillations. Therefore, under unknown parameter deviations, relying only on nominal conditions or manual experience is insufficient to obtain control performance that is satisfactory over multiple conditions. Based on this consideration, the next section formulates dual-loop FOPI parameter tuning as a multi-condition optimization problem and uses PSO for offline optimization.

## 3. Multi-Condition PSO-Based FOPI Parameter-Tuning Method

### *3.1. Parameterization of the Dual-Loop FOPI Controller*

The proposed control structure consists of a voltage loop and a current-sharing loop. If the proportional gain, integral gain, and additional fractional order of the two FOPI controllers are directly optimized, the optimization vector can be expressed as: $\Theta = [K_{pv}, K_{iv}, \lambda_v, K_{pi}, K_{ii}, \lambda_i]$, where the subscripts $v$ and $i$ denote the voltage loop and current-sharing loop, respectively, $\lambda_v$ and $\lambda_i$ denote the additional fractional orders of the two FOPI controllers. This parameter form is intuitive, but the parameters differ greatly in magnitude, especially because the proportional and integral gains may differ by several orders of magnitude, reducing the search efficiency of PSO. Therefore, this paper adopts a frequency-domain feature-based parameterization method, in which the magnitude, phase angle, and additional fractional order of each controller at a specified reference frequency are used as the optimization variables.

For the voltage loop and current-sharing loop, the reference frequencies $f_{0v}$ and $f_{0i}$ are selected respectively. Considering that the voltage loop mainly regulates the output voltage and is affected by the output capacitor and load energy stabilization, its response is relatively slow; the current-sharing loop mainly suppresses the two-phase current difference and usually requires a faster dynamic response. Thus, $f_{0v}$ is generally chosen to be lower than $f_{0i}$ . The particle position is defined as: $X = [G_v, \varphi_v, \lambda_v, G_i, \varphi_i, \lambda_i]$, where $G_v$ and $\varphi_v$ denote the magnitude and phase of the voltage-loop controller at the reference frequency, $\lambda_v$ is the additional fractional order of the voltage-loop controller, and $G_i$, $\varphi_i$ and $\lambda_i$ are the corresponding quantities for the current-sharing loop. The actual integral orders implemented in the voltage and current-sharing loops are therefore $1+\lambda_v$ and $1+\lambda_i$, respectively. Before each fitness evaluation, the frequency-domain feature parameters provided by the particle are converted back into the actual proportional and integral gains of the FOPI controller. If the resulting $K_p$ or $K_i$ violates the specified bounds, the particle is treated as invalid.

### *3.2. Particle Swarm Optimization Process*

Particle swarm optimization is a stochastic optimization method based on population search. Each particle represents a candidate set of controller parameters. During the search, each particle updates its position according to its own historical best position and the global best position of the population, gradually converging toward a better solution.

Let the position and velocity of the *q*-th particle at the *r*-th iteration be $X_q^r$ and $V_q^r$, respectively. Let $P_q^r$ be its personal best position and $G^r$ be the global best position. The velocity and position update equations are:

$$\begin{gathered} V_q^{r+1} = \omega V_q^r + c_1 r_1 (P_q^r - X_q^r) + c_2 r_2 (G^r - X_q^r) \\ X_q^{r+1} = X_q^r + V_q^{r+1} \end{gathered} \tag{11}$$

where $\omega$ is the inertia weight, $c_1$ and $c_2$ are learning factors, $r_1$ and $r_2$ are random numbers in $[0,1]$. The inertia weight preserves the original search direction of the particle, while the learning factors describe the attraction of the particle toward its personal best and the global best positions.

In this work, each particle represents one set of frequency-domain feature parameters for the dual-loop FOPI controllers. For each particle, the position variables are first converted into the actual controller parameters of the voltage and current-sharing loops. The parameters are then written into the Simulink closed-loop model of the parallel LLC converter, and simulations are run under multiple parameter-deviation conditions. After each simulation, the time-domain responses of the output-voltage error and current-sharing error are used to calculate the fitness score of the particle. A lower fitness score indicates better comprehensive performance under the current evaluation criteria.

To improve the initial search efficiency, a seed particle based on controller parameters obtained from experience or nominal-condition tuning is included during PSO initialization, allowing the algorithm to begin searching from a relatively reasonable region. The population size is set to 48 and the maximum number of iterations is set to 40. The remaining particles are randomly distributed within the specified bounds to maintain a certain global search capability. PSO is used only for offline parameter tuning. In the actual hardware, only the optimized fixed controller parameters are executed, and the PSO algorithm is not run online. The optimization process is shown in Figure 3.

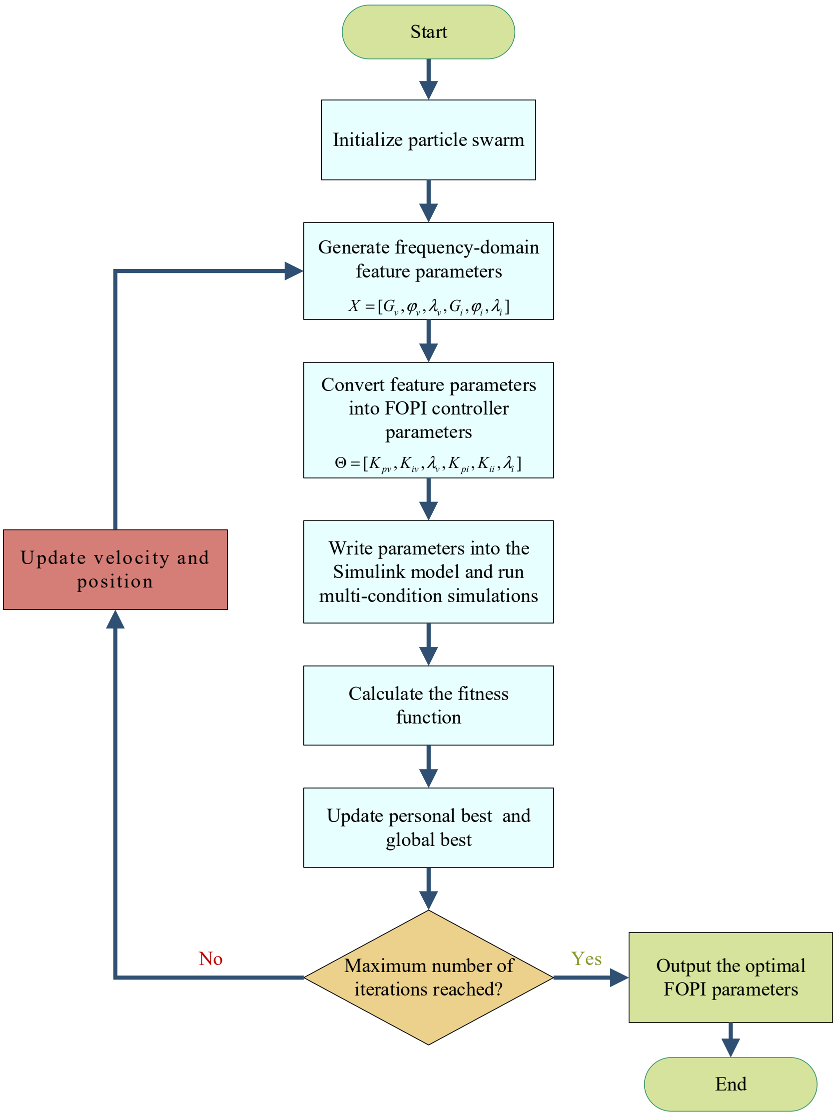


**Figure 3.** Offline tuning process of the dual-loop FOPI parameters based on PSO.

### *3.3. Construction of the Multi-Condition Set*

The control performance of a parallel LLC converter is jointly affected by variations in the resonant inductor, resonant capacitor, magnetizing inductor, and load. If the controller is designed only under the nominal condition, the obtained parameters may be suitable only for a single operating point and may lead to slower responses, larger overshoots, or stronger oscillations under other parameter-deviation conditions. Therefore, this paper transforms controller tuning into a multi-condition optimization problem. Let the condition set be $\Omega=\{\Omega_1,\Omega_2,\cdots,\Omega_N\}$, where each condition represents a set of LLC parameters. For a two-phase parallel LLC converter, the parameters can be written as $\Omega_j=[L_{r1},C_{r1},L_{m1},L_{r2},C_{r2},L_{m2}]_j$. Because this paper focuses on the influence of unknown resonant-tank parameter deviations on current-sharing control, six representative single-parameter deviation conditions are selected as the training conditions. Specifically, $L_{r1}$, $C_{r1}$, and $L_{m1}$ of Phase 1 are individually decreased by 15%, while $L_{r2}$, $C_{r2}$, and $L_{m2}$ of Phase 2 are individually increased by 15%, with all other parameters kept at their nominal values. Since the two LLC phases are structurally identical in the nominal model, interchanging the phase indices gives the corresponding mirrored deviation conditions. Therefore, the six conditions in Table 1 are selected to represent the two deviation directions without introducing redundant phase-swapped cases. The nominal condition is not included as a training condition because, with identical resonant-tank parameters in the two phases, no parameter-induced current imbalance is present and the two phases naturally share the load current. More general cases, including simultaneous deviations of multiple parameters and combinations of positive and negative deviations in the two phases, are further evaluated by the Monte Carlo simulations in Section 4.3. Table 1 summarizes the six representative training conditions, with all parameters normalized to their nominal values.

**Table 1.** Parameter settings of the six representative training conditions relative to the nominal values.

| Condition | $L_{r1}$ | $C_{r1}$ | $L_{m1}$ | $L_{r2}$ | $C_{r2}$ | $L_{m2}$ |
|---|---|---|---|---|---|---|
| C1 | 0.85 | 1.0 | 1.0 | 1.0 | 1.0 | 1.0 |
| C2 | 1.0 | 0.85 | 1.0 | 1.0 | 1.0 | 1.0 |
| C3 | 1.0 | 1.0 | 0.85 | 1.0 | 1.0 | 1.0 |
| C4 | 1.0 | 1.0 | 1.0 | 1.15 | 1.0 | 1.0 |
| C5 | 1.0 | 1.0 | 1.0 | 1.0 | 1.15 | 1.0 |
| C6 | 1.0 | 1.0 | 1.0 | 1.0 | 1.0 | 1.15 |

### *3.4. Design of the Multi-Condition Fitness Function*

To ensure that the optimized controller is not only suitable for a single nominal condition but also maintains acceptable performance under multiple parameter-deviation conditions, a worst-case evaluation strategy is adopted in this paper. For each particle, closed-loop simulations are performed under N parameter-deviation conditions, and the corresponding single-condition score $J_i$ is calculated for each condition. The total fitness of the particle is then defined as the maximum score among all conditions:

$$J(X) = \max_{\Omega_j \in \Omega} J_j(X) \tag{12}$$

This strategy prevents the optimization algorithm from obtaining good results only for an easy condition while ignoring stability and dynamic performance under extreme deviation conditions.

For the *j*-th condition, the single-condition score is constructed based on the output-voltage error and the current-sharing error. A deadband is introduced to avoid excessive sensitivity to small steady-state errors and measurement noise. Let $e(t)$ be the original error and *db* be the deadband threshold. In this paper, the voltage-error deadband is set to 0.1%, and the current-sharing-error deadband is set to 1%. The effective error is defined as:

$$e_{eff}(t) = \max(|e(t)| - db, 0) \tag{13}$$

When the error lies inside the deadband, no additional fitness penalty is imposed. Only the portion exceeding the deadband is included in the performance evaluation. This treatment prevents the controller from being over-optimized for measurement noise or small steady-state deviations.

The single-condition score consists of four types of performance indicators.

First, the steady-state error indicator is used to evaluate whether the system finally converges to the neighborhood of the deadband. Let $[N_1, N_2]$ denote the final evaluation window. The steady-state error indicator is defined as:

$$J_{sse} = \frac{1}{N_2 - N_1 + 1} \sum_{k=N_1}^{N_2} e_{eff}(k) \tag{14}$$

Second, the time-weighted error integral indicator is used to evaluate the convergence speed of the error:

$$J_{ITAE} = \frac{\sum_{k=1}^{N} kT_s e_{eff}(k)}{Limit_{ITAE}} \tag{15}$$

where $T_s$ is the sampling period, and $Limit_{ITAE}$ is a preset normalization limit used to keep the numerical magnitudes of different indicators comparable. This indicator assigns a larger penalty to errors that remain in the later stage of the response, thereby constraining the response speed of the controller and avoiding overly conservative optimization results.

Third, the peak violation indicator is used to evaluate the maximum amount by which the error exceeds the deadband during the transient process:

$$J_{os} = \max_{1 \le k \le N} e_{eff}(k) \tag{16}$$

This indicator prevents the optimization algorithm from selecting overly aggressive controller parameters that achieve fast responses at the cost of excessive overshoot.

Fourth, the oscillation indicator is used to evaluate the smoothness of the error-convergence process. It is described by the variation path length of the effective error:

$$J_{osc} = \frac{\sum_{k=2}^{N} | e_{eff}(k) - e_{eff}(k-1)|}{| e_{eff}(N) - e_{eff}(1) |} - 1 \tag{17}$$

This indicator suppresses persistent ringing and repeated crossings of the deadband, helping PSO obtain smoother and more stable control responses.

By combining the voltage-loop and current-sharing-loop indicators, the single-condition score of the jth condition is defined as:

$$\begin{aligned} J_j = \; & w_{v1}J_{ss,v} + w_{v2}J_{ITAE,v} + w_{v3}J_{os,v} + w_{v4}J_{osc,v} \\ & + w_{i1}J_{ss,i} + w_{i2}J_{ITAE,i} + w_{i3}J_{os,i} + w_{i4}J_{osc,i} \end{aligned} \tag{18}$$

where the subscript $v$ denotes the voltage-error indicators, the subscript $i$ denotes the current-sharing-error indicators, and $w_{v1} \sim w_{i4}$ are the corresponding weighting coefficients. In this paper, all weighting coefficients are set to 100. Through the proposed fitness function, PSO simultaneously considers voltage-regulation performance, current-sharing performance, response speed, and oscillation suppression under multiple operating conditions, thereby avoiding degradation in one performance aspect caused by optimizing only another. In addition, if output-voltage runaway, frequency-command saturation, error divergence, or simulation failure occurs during a simulation, the corresponding particle is assigned a large penalty value to ensure that the obtained controller parameters satisfy basic engineering constraints.

## 4. Simulation and Experimental Verification

The verification in this section follows the control signal chain established in Sections 2 and 3. The measured or simulated output voltage and two phase output currents are first used to obtain the filtered voltage and current signals, from which the voltage-loop error and current-sharing-loop error are calculated. These two errors are then processed by the dual-loop FOPI controllers to generate the common-mode and differential-mode frequency corrections, which are finally synthesized into the switching frequencies of the two LLC phases. Therefore, the following simulation and hardware results are used to verify different parts of the proposed control framework: the training-condition simulations verify the dynamic response under typical resonant-parameter deviations, the Monte Carlo simulations evaluate the adaptability over a random parameter-deviation range, and the hardware experiment verifies the practical implementation of the optimized controller on a digital control platform.

### *4.1. Simulation Model and Parameter Settings*

To verify the proposed control strategy, a closed-loop simulation model of the two-phase parallel LLC resonant converter is established in MATLAB/Simulink. The sampling frequency and control frequency are both 100 kHz. The FOPI parameters in the control system are obtained offline using the PSO method described in Section 3.

To separately observe voltage regulation, current-sharing regulation, and load-disturbance recovery, the simulation sequence is set as follows: the voltage loop is enabled at $t$ = 0.02 s, the current-sharing loop is enabled at $t$ = 0.03 s, and the load is switched from half load to full load at $t$ = 0.04 s. The simulation parameters and control parameters are shown in Table 2. The resonant-parameter deviation settings of the training conditions are consistent with Table 1.

**Table 2.** Simulation parameter settings.

| Parameter | Value | Parameter | Value |
|---|---|---|---|
| Input voltage Vin | 400 V | Resonant inductors $L_{r1}/L_{r2}$ | 33.6 μH (±15%) |
| Transformer turns ratio $n$ | 4:1 | Resonant capacitors $C_{r1}/C_{r2}$ | 33 nF (±15%) |
| Current-sensor cutoff frequency | 16 kHz | Magnetizing inductors $L_{m1}/L_{m2}$ | 307.7 μH (±15%) |
| Voltage-sensor cutoff frequency | 16 kHz | Load resistance $R_L$ | 5.0/2.5 Ω (half/full load) |
| Control frequency | 100 kHz | Rated power $P$ | 500 W/1000 W (half/full load) |
| $K_{p,v}$ | 0.6115 | $K_{p,i}$ | 0.0334 |
| $K_{i,v}$ | 4935 | $K_{i,i}$ | 515 |
| $1+\lambda_v$ | 1.365 | $1+\lambda_i$ | 1.078 |

### *4.2. Dynamic Response Verification under Training Conditions*

Figure 4 shows the voltage-error and current-sharing-error responses under the six training conditions. Figure 4a shows the overall voltage-error response, while Figure 4b–d show the enlarged voltage-error responses during voltage-loop startup, current-sharing-loop startup, and load switching, respectively. Figure 4e shows the overall current-sharing-error response, while Figure 4f,g show the enlarged current-sharing-error responses during current-sharing-loop startup and load switching, respectively. The six conditions correspond to $L_{r1}$−15%, $C_{r1}$−15%, $L_{m1}$−15%, $L_{r2}$+15%, $C_{r2}$+15%, and $L_{m2}$+15%, respectively. All conditions use the same set of PSO-FOPI controller parameters.

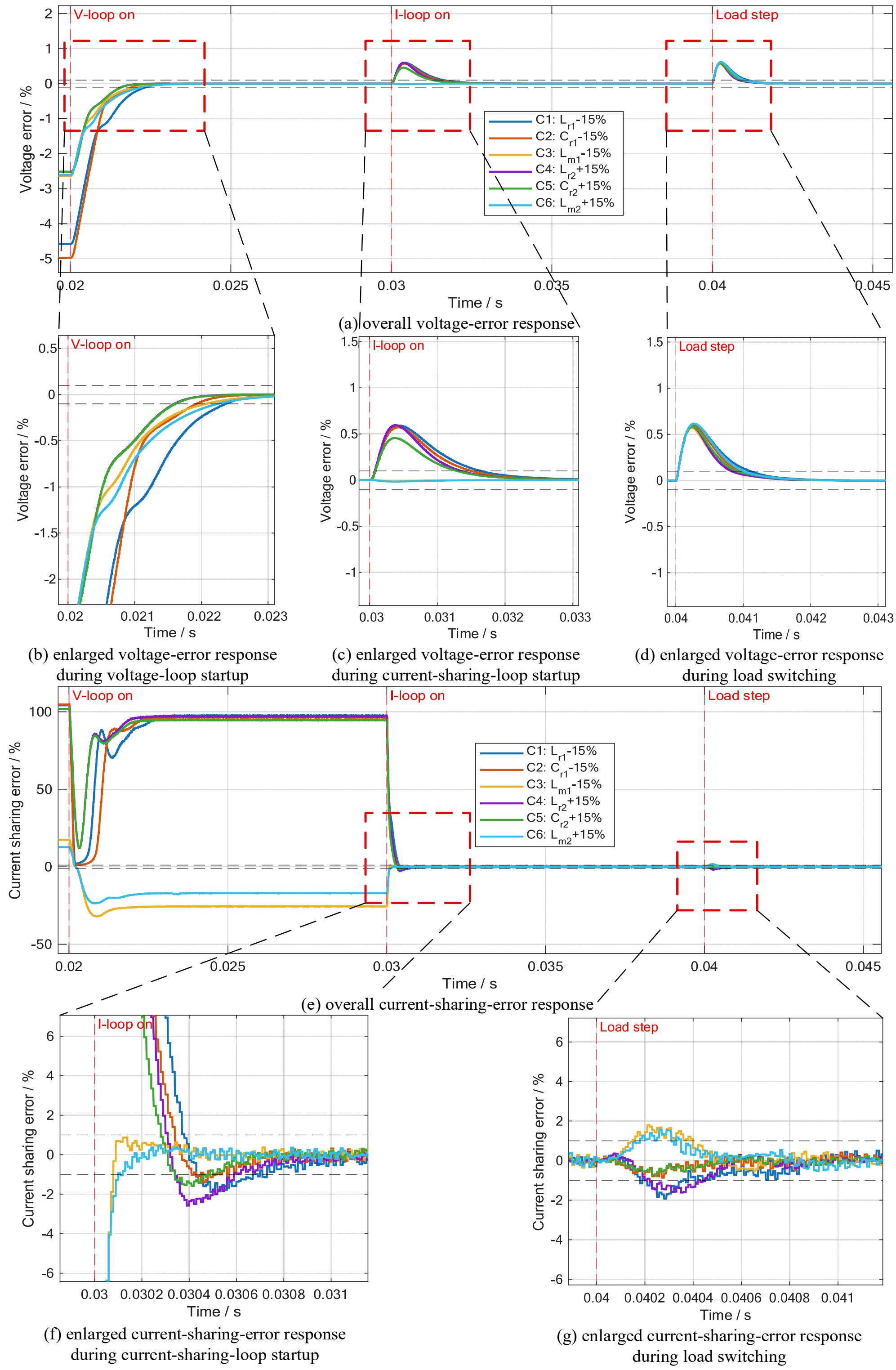


**Figure 4.** Voltage-error and current-sharing-error responses under the six training conditions.

After the voltage loop is enabled at $t = 0.02$ s, the voltage error under all conditions converges to within the ±0.1% deadband within 2.5 ms, without obvious positive overshoot. This result indicates that common-mode frequency regulation can maintain favorable voltage-regulation dynamic performance under typical resonant-parameter deviations. After the current-sharing loop is enabled at $t = 0.03$ s, the two-phase current error rapidly converges from the initial unbalanced state to within the ±1% deadband. The settling time is less than 1 ms and the current-sharing overshoot is less than 3%. This result shows that differential-mode frequency regulation can effectively compensate for the interphase power-distribution difference caused by parameter deviations.

During current-sharing-loop startup, the voltage error exhibits only a short disturbance of about 0.5% and quickly returns near the voltage deadband, indicating that differential-mode frequency regulation has little influence on the common output voltage. After the load is switched from half load to full load at $t = 0.04$ s, the voltage-error peak is about 0.6% and the current-sharing-error peak is about 2%; both quickly recover to the corresponding deadband ranges. Therefore, under the six typical parameter-deviation conditions, the same set of PSO-FOPI parameters can simultaneously satisfy the requirements of voltage regulation, current-sharing regulation, and load-disturbance recovery.

### *4.3. Monte Carlo Simulation Verification under a ±15% Parameter-Deviation Range*

To further evaluate the adaptability of the proposed controller to unknown resonant-parameter deviations, Monte Carlo random-parameter simulations are performed. The random variables are the resonant inductors, resonant capacitors, and magnetizing inductors of the two LLC phases. Each parameter varies independently within ±15% of its nominal value, and 100 random conditions are generated. The same set of PSO-FOPI controller parameters is used for all random conditions.

Figure 5 shows the dynamic-performance distributions under Monte Carlo random parameter-deviation conditions. Figure 5a shows the voltage settling-time distribution, Figure 5b shows the current-sharing settling-time distribution, Figure 5c shows the current-sharing overshoot distribution, and Figure 5d shows the current-sharing error recovery-time distribution after the load step. The voltage settling time is mainly concentrated within 1–2.5 ms, with a mean value of approximately 1.79 ms. The current-sharing settling time is mainly concentrated within 0.2–0.6 ms, with a mean value of approximately 0.416 ms. The current-sharing overshoot is mainly concentrated within 1–2.5%, with a mean value of approximately 1.55%. During the load step, the current-sharing error remains within the ±1% deadband for some random cases; therefore, a relatively large number of cases in Figure 5d have a recovery time of 0. For the remaining cases, the current-sharing error quickly re-enters the deadband after the load step, with a mean recovery time of approximately 0.204 ms and a 95th-percentile value of approximately 0.471 ms. Because the voltage overshoot is relatively small, its distribution is not plotted separately.

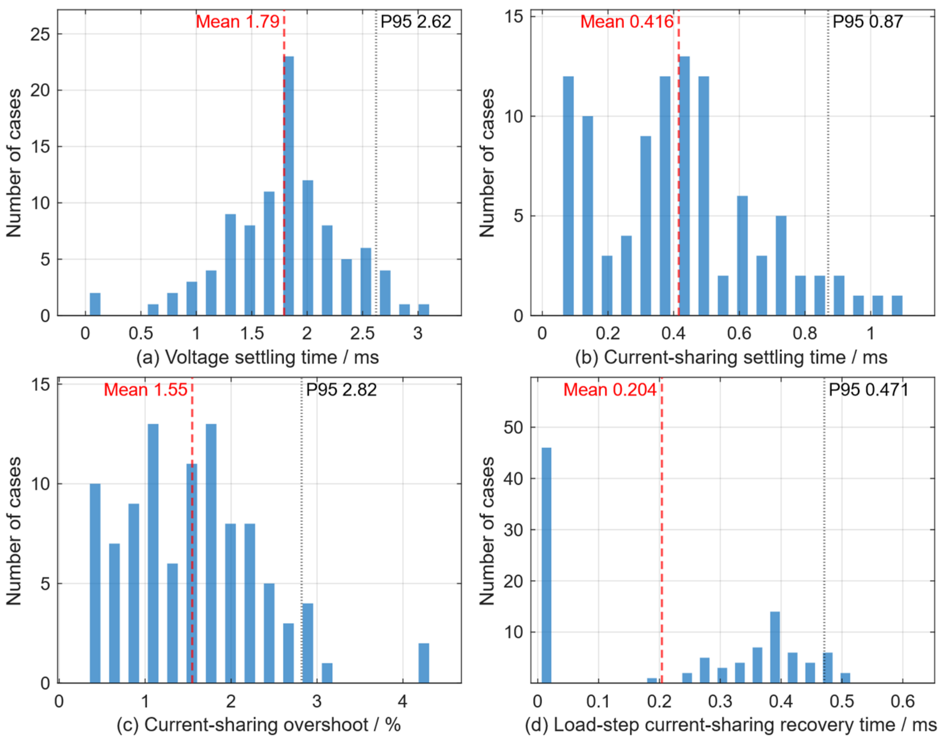


**Figure 5.** Dynamic-performance distributions under Monte Carlo random parameter-deviation conditions.

These statistical results show that within the ±15% random resonant-parameter deviation range, the voltage settling time, current-sharing settling time, and current-sharing overshoot remain relatively concentrated, and no obvious abnormal conditions occur. Compared with the six training conditions, the Monte Carlo results further indicate that the proposed PSO-FOPI controller is not effective only for specific parameter-deviation cases, but also has good multi-condition adaptability and dynamic stability within the specified deviation range.

### *4.4. Experimental Verification*

A two-phase parallel LLC experimental platform is built based on the simulation parameters. Figure 6 shows the experimental prototype. The platform consists of a DC power supply, electronic load, oscilloscope, two-phase parallel LLC power circuit, and DSP control board. The power switches are SCT30N120 devices, the rectifier diodes are MUR3020PT devices, and the controller is implemented using a TMS320F28335. Both the control frequency and sampling frequency are 100 kHz. In the experiment, the first phase uses the nominal resonant-tank parameters, whereas the resonant capacitor $C_{r2}$ of the second phase is increased by 15% to emulate a representative parameter-deviation condition. In the simulations, deviations of $L_r$, $C_r$, and $L_m$ have been evaluated through the six typical parameter-deviation conditions and the ±15% Monte Carlo random parameter-deviation analysis. In the hardware experiment, $C_{r2}$ is selected as a controllable and repeatable representative case because physically changing the resonant or magnetizing inductors is less practical and may introduce additional parasitic variations.

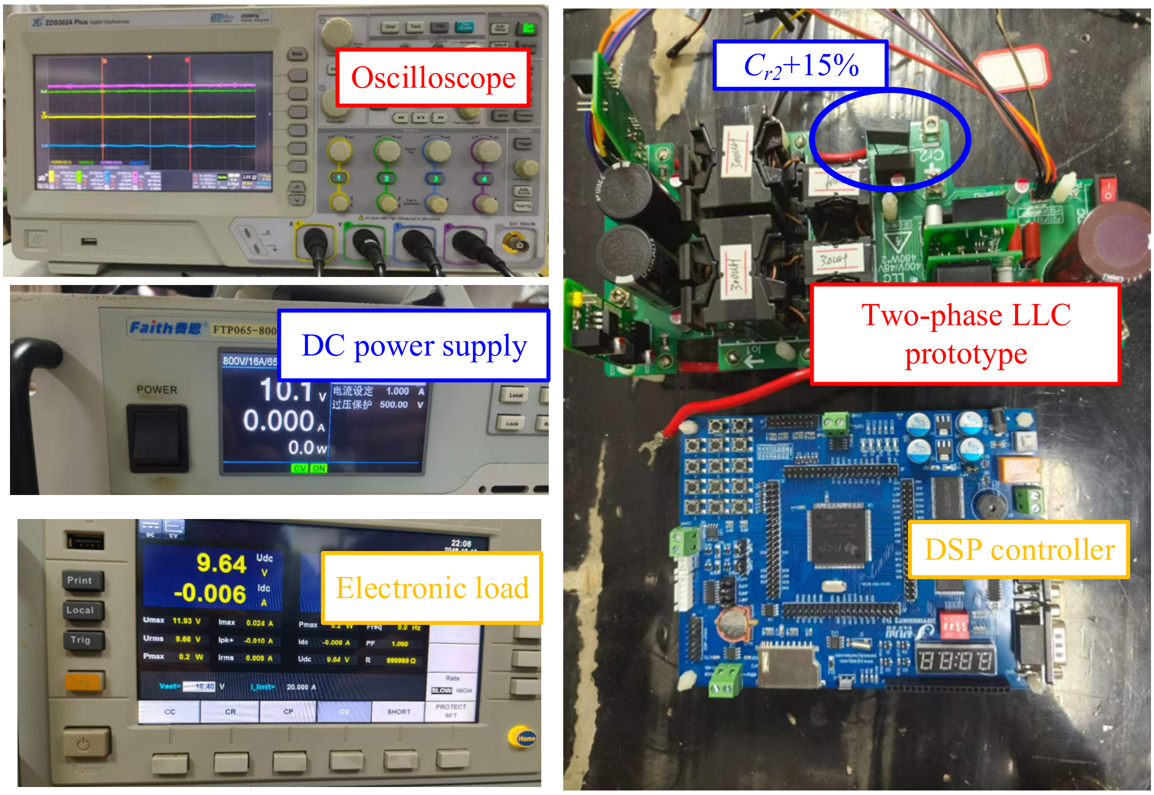


**Figure 6.** Two-phase parallel LLC experimental platform.

Figure 7 shows the experimental voltage and current response waveforms. Figure 7a corresponds to the operation with only the voltage loop enabled. The output voltage stabilizes near the reference value within about 2.8 ms, but the two phase currents still exhibit an obvious deviation. This result indicates that the voltage loop can regulate the common output voltage but cannot actively eliminate the current imbalance caused by parameter deviation. Figure 7b corresponds to the current-sharing-loop startup process. The two phase output currents converge within about 900 µs, the steady-state current-sharing error is less than 1%, and the output voltage exhibits no obvious dip or oscillation. This result indicates that the current-sharing loop can rapidly regulate current distribution and has little effect on the voltage loop.

Figure 7c,d correspond to load switching from half load to full load and from full load to half load, respectively. It should be noted that the current-sharing loop is already enabled in these experiments; therefore, the two phase currents remain well balanced before and after load switching. The annotated time of about 12 µs mainly corresponds to the visible transition time during which the output current changes from the half-load level to the full-load level, or returns from the full-load level to the half-load level. It is not the complete regulation time for the current-sharing loop to re-establish current sharing from an unbalanced state. The waveforms show that during load switching, the output voltage remains close to 50 V, and the two phase output currents change synchronously without obvious sustained oscillation or current-sharing instability. This result indicates that, under the present experimental condition, the proposed dual-loop controller maintains favorable voltage-regulation and current-sharing operation during load disturbances.

To evaluate the influence of current-sharing control on the efficiency of the experimental prototype, the conversion efficiencies under half-load and full-load conditions are measured for operation with only the voltage loop and with the current-sharing loop enabled. The experimental results show that, after the current-sharing loop is enabled, the system efficiency increases by about 1.00 percentage point under half load and by about 0.74 percentage point under full load; the full-load efficiency with current sharing reaches about 95.34%. This result suggests that when parameter deviation causes unequal current distribution between the phases, current-sharing control can improve the power-sharing relationship and provide a certain efficiency improvement in the experimental prototype.

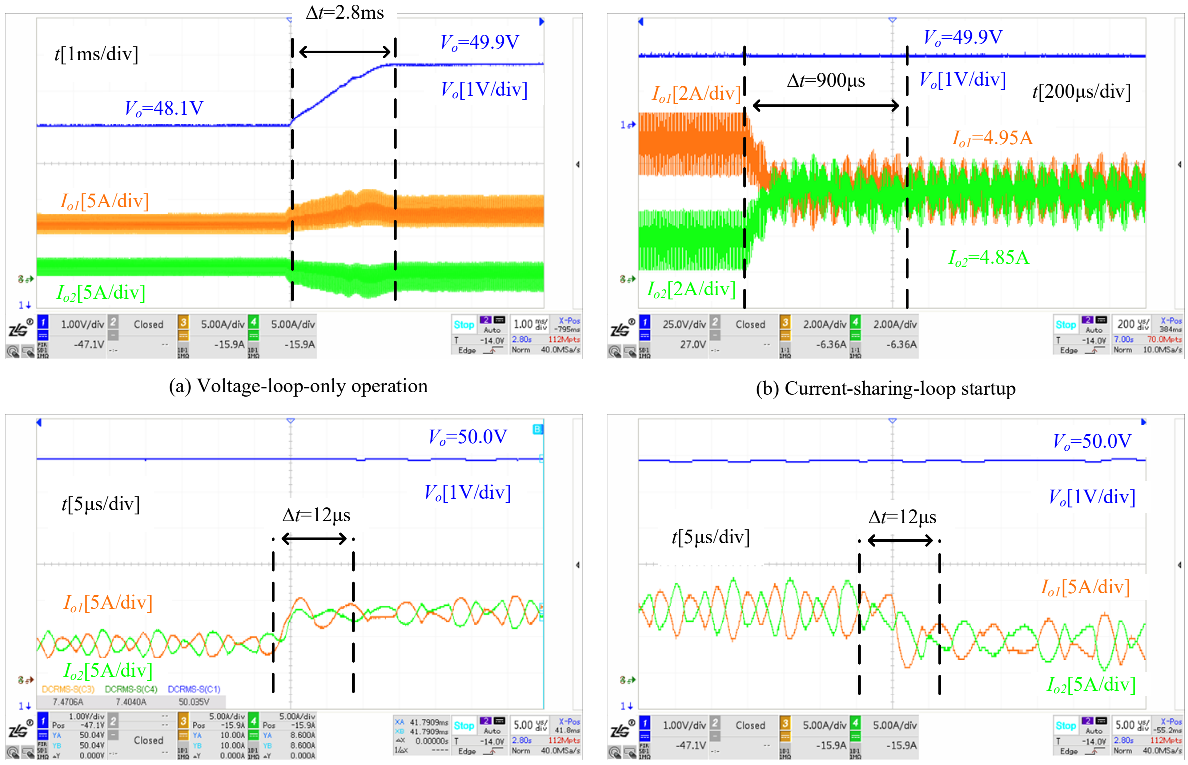


(a) Voltage-loop-only operation

(b) Current-sharing-loop startup

(c) Half-load to full-load switching

(d) Full-load to half-load switching

**Figure 7.** Experimental voltage and current response waveforms.

## 5. Discussion

Existing active current-sharing methods without auxiliary power devices can correct interphase power distribution by regulating the duty cycle, phase-shift angle, or switching frequency without changing the main LLC power topology, and can achieve good current-sharing performance. Table 3 compares related active current-sharing methods without auxiliary power devices in terms of parameter-deviation range, current-sharing performance, and dynamic verification. Existing methods can achieve small steady-state current-sharing errors without adding extra power devices and can maintain fast dynamic responses under load-switching conditions. Compared with these methods, the focus of this paper is not to obtain the shortest load-switching time under a single operating condition, but to formulate the parameter tuning of the common-mode/differential-mode dual-loop FOPI controller as a multi-condition optimization problem and to verify its dynamic adaptability under six typical parameter-deviation conditions and a ±15% Monte Carlo random parameter-deviation range. The results show that the voltage error can be reduced to within the ±0.1% deadband within 2.5 ms, the current-sharing error can be reduced to within the ±1% deadband within 1 ms, and the current-sharing overshoot is less than 3%. In the Monte Carlo simulation, the mean current-sharing recovery time after the load step is approximately 0.204 ms, and the 95th-percentile value is approximately 0.471 ms. These results indicate that the proposed method can maintain favorable voltage regulation, current-sharing, and load-disturbance recovery performance within the specified resonant-parameter-deviation range.

In addition, this paper treats the “current-sharing-loop startup dynamics” and the “load-switching dynamics” as two different processes. The current-sharing-loop startup dynamics characterize the ability of the system to converge from a parameter-deviation-induced unbalanced state to a balanced state; in the hardware experiment, the two phase currents converge within about 900 μs and the steady-state current-sharing error is less than 1%. By contrast, the load-switching dynamics are evaluated when the current-sharing loop has already been enabled, and are mainly used to verify whether the system can maintain voltage regulation and current sharing during load disturbances. The Monte Carlo results show that, in some random conditions, the current-sharing error never exceeds the ±1% deadband after load switching, indicating that load disturbances do not necessarily break the current-sharing state. In the remaining conditions, the current-sharing error also re-enters the deadband quickly.

Although the above results verify the effectiveness of the proposed method within the specified resonant-tank parameter-deviation range, there remains room for further improvement. The controller parameters are obtained mainly through offline optimization, and their performance depends on the consistency between the simulation model and the practical system. In future work, online parameter identification, adaptive updating, or model predictive control may be combined with the proposed method so that the controller can dynamically adjust according to the actual resonant-tank state, further improving its adaptability under wider parameter variations and more complex operating conditions.

**Table 3.** Performance comparison of active current-sharing methods without auxiliary power devices.

| Reference | Parameter Deviation | Extra Power Devices Required? | Current-Sharing Performance | Dynamic Process from Unbalanced to Balanced State | Load-Switching Verification |
|---|---|---|---|---|---|
| [24] | 6.4%, 9.1% | No | 2.22% | 20ms | Not demonstrated |
| [20] | 15% | No | 1.5% | Not demonstrated | About 10 ms |
| [17] | 5% | No | <1% | Not demonstrated | About 300 μs |
| [21] | 5% | No | <1% | Not demonstrated | About 300 μs |
| This paper | 15% | No | 1% | 900 μs | P95 471 μs; mean 204 μs |

Note: “mean” and “P95” are obtained from the Monte Carlo simulations under multiple random parameter-deviation cases. “Mean” denotes the arithmetic mean value, and “P95” denotes the 95th-percentile value.

## 6. Conclusions

This paper proposes a multi-condition PSO-FOPI current-sharing control method for parallel LLC resonant converters under resonant-tank parameter deviations. The proposed method adopts a common-mode/differential-mode frequency dual-loop structure, in which the common-mode frequency regulates the common output voltage and the differential-mode frequency regulates the two-phase output-current distribution. PSO is used to offline optimize the dual-loop FOPI controller parameters.

The results show that, within the ±15% resonant-tank parameter-deviation range, the proposed method achieves favorable voltage-regulation and current-sharing dynamic performance. The voltage error can be reduced to within the ±0.1% deadband within 2.5 ms, the current-sharing error can be reduced to within the ±1% deadband within 1 ms, and the current-sharing overshoot is less than 3%. After the load step, the mean current-sharing error recovery time is approximately 0.204 ms, indicating that the proposed controller still has favorable load-disturbance recovery capability under random parameter deviations. Hardware experiments further demonstrate the feasibility of implementing the proposed controller on a DSP platform.

## 7. Biographies of the Authors

Shicheng Yang received his B.Eng. degree in Civil Engineering from Tongji University, Shanghai, China. He is currently pursuing his M.Sc. degree at Xiamen University, Xiamen, China. His main research interests include DC–DC resonant converters, parallel converter current-sharing control, and power electronic system modeling.

Liangzong He was born in Hunan, China, in 1984. He received the B.Sc. degree from Jilin University, Changchun, China, in 2006, and the Ph.D. degree from Huazhong University of Science and Technology, Wuhan, China, in 2012, both in electrical engineering. In 2012, he joined Xiamen University, Xiamen, China, as an Assistant Professor, where he has been a Professor since 2019. From 2009 to 2011, he was a joint Ph.D. student with Michigan State University, East Lansing, MI, USA. His research interests include fractional-order power electronics technology and intelligent power electronics technology, as well as their applications in wireless power transfer systems.

Jian Ye, Professor, MoE Key Laboratory of Human Factors and Intelligent Reduction of Vibration & Noise, China, Fuyao University of Science and Technology, Fuzhou 350000, China

## Author Contributions

S.Y.: conceptualization, methodology, software, investigation, validation, formal analysis, visualization, writing—original draft preparation. L.H.: supervision, project administration, methodology review, writing—review and editing. J.Y.: supervision, writing—review and editing. All authors have read and agreed to the published version of the manuscript.

## Funding

This research received no external funding.

## Institutional Review Board Statement

Not applicable.

## Informed Consent Statement

Not applicable.

## Data Availability Statement

The data presented in this study are available from the corresponding author upon reasonable request.

## Conflicts of Interest

L.H. is an Editorial Board Member of *Power Electronics Research and Applications Transactions*. Given this role, L.H. had no involvement in the peer review of this paper and had no access to information regarding its peer-review process. Full responsibility for the editorial process of this paper was delegated to another editor of the journal. The authors declare no other conflicts of interest.

## Use of AI and AI-Assisted Technologies

During the preparation of this work, the authors used AI-assisted tools for language polishing and translation. After using these tools, the authors reviewed and edited the content as needed and take full responsibility for the content of the published article.

## References

1. Zeng, J.; Zhang, G.; Yu, S.S.; et al. LLC Resonant Converter Topologies and Industrial Applications—A Review. *Chin. J. Electr. Eng.* **2020**, *6*, 73–84. https://doi.org/10.23919/cjee.2020.000021.
2. Guimarães França, J.V.; Costa, L.F.; Papafotiou, G. A Highly Modular Interphase Solid-State Transformer Architecture. In Proceedings of the 2025 IEEE Energy Conversion Conference Congress and Exposition (ECCE), Philadelphia, PA, USA, 19–23 October 2025; pp. 1–8. https://doi.org/10.1109/ecce58356.2025.11259843.
3. França, J.V.G.; Christou, I.; van de Zanden, M.; et al. A Highly Modular LLC-based Interphase Solid-State Transformer Architecture for Smart-Grid Applications. *IEEE Trans. Power Electron.* **2026**. 1–15. https://doi.org/10.1109/tpel.2026.3716728.
4. Dong, H.; Xie, X. Review of Current-Sharing Schemes for Multiphase LLC Resonant Converter. *IEEE Trans. Power Electron.* **2025**, *40*, 1322–1345. https://doi.org/10.1109/tpel.2024.3447047.
5. Shah, S.S.; Rastogi, S.K.; Bhattacharya, S. Paralleling of LLC Resonant Converters. *IEEE Trans. Power Electron.* **2021**, *36*, 6276–6287. https://doi.org/10.1109/tpel.2020.3040621.
6. Sun, Z.; Wu, Q.; Wang, Q.; et al. An Improved Grouping Transformer's Secondary Windings Current-Sharing Method for Multiphase LLC Converter. *IEEE Trans. Power Electron.* **2023**, *38*, 9872–9884. https://doi.org/10.1109/tpel.2023.3271351.
7. Sun, Z.; Wang, Q.; Wu, Q.; et al. A Unified Common Inductor and Common Capacitor Current Sharing Method for Multiphase LLC Converter. *IEEE Trans. Power Electron.* **2022**, *37*, 12182–12196. https://doi.org/10.1109/tpel.2022.3178497.
8. Kim, T.; Choi, D.; Choi, S.H.; et al. Improved Natural Current Sharing and Phase-Shedding Operation in LLC Resonant Converters with Voltage-Doubler Rectifier. *IEEE Trans. Power Electron.* **2024**, *39*, 13401–13412. https://doi.org/10.1109/tpel.2024.3422316.

9. Sun, Z.; Yang, Y.; Zeng, J.; et al. Coupled Resonant Tank Current-Sharing Topology for Multiphase LLC-DCX Converter with Phase-Shedding Ability. *IEEE J. Emerg. Sel. Top. Power Electron.* **2025**, *13*, 7297–7313. https://doi.org/10.1109/jestpe.2025.3607893.
10. Hu, Z.; Qiu, Y.; Wang, L.; et al. An Interleaved LLC Resonant Converter Operating at Constant Switching Frequency. *IEEE Trans. Power Electron.* **2014**, *29*, 2931–2943. https://doi.org/10.1109/tpel.2013.2273939.
11. Zhou, X.; Yu, X.; Li, C.; et al. A Reduced-Switch-Count Two-Phase Interleaved Switch-Control-Capacitor LLC Converter with Accurate Current Balancing. *IET Power Electron.* **2024**, *17*, 1163–1175. https://doi.org/10.1049/pel2.12467.
12. Dong, H.; Xie, X. A Novel Current Sharing Scheme for Multiphase Interleaved LLC Converter Based on Partial Energy Regulation of Resonant Capacitor. *IEEE J. Emerg. Sel. Top. Power Electron.* **2025**, *13*, 136–146. https://doi.org/10.1109/jestpe.2024.3480956.
13. Liu, K.; Xiao, T.; Zhao, J.; et al. Differentiated-Gain-Regulation-Based Current Balancing Control for Multi-Phase Interleaved LLC Resonant Converters. *IEEE Open J. Power Electron.* **2025**, *6*, 1428–1437. https://doi.org/10.1109/ojpel.2025.3600380.
14. Cheng, Z.; He, L.; Yang, H. Fewer-Sensors Current Balancing in LLC-DCX Converters Parallel System with Powerless Fractional-Order Capacitor. *IEEE Trans. Transp. Electrif.* **2026**, *12*, 464–473. https://doi.org/10.1109/tte.2025.3616127.
15. Zong, S.; Luo, H.; Li, W.; et al. Theoretical Evaluation of Stability Improvement Brought by Resonant Current Loop for Paralleled LLC Converters. *IEEE Trans. Ind. Electron.* **2015**, *62*, 4170–4180. https://doi.org/10.1109/tie.2014.2385661.
16. Murata, K.; Kurokawa, F. An Interleaved PFM LLC Resonant Converter with Phase-Shift Compensation. *IEEE Trans. Power Electron.* **2016**, *31*, 2264–2272. https://doi.org/10.1109/tpel.2015.2427735.
17. Moreno, M.; Pereda, J.; Rojas, F.; et al. Decoupled PI Controllers Based on Pulse-Frequency Modulation for Current Sharing in Multi-Phase LLC Resonant Converters. *IEEE Access* **2021**, *9*, 15283–15294. https://doi.org/10.1109/access.2021.3053171.
18. Wang, Y.; Ren, X.; Zhang, Z.; et al. Research on Current Sharing Strategy of Parallel LLC Resonant Converter. In Proceedings of the 2019 IEEE Applied Power Electronics Conference and Exposition (APEC), Anaheim, CA, USA, 17–21 March 2019. https://doi.org/10.1109/apec.2019.8721775.
19. Zhang, C.; Duan, B.; Song, J.; et al. A Modified Active Disturbance Rejection Control Strategy for Current Balance in Parallel LLC Resonant Converter. In Proceedings of the 2022 34th Chinese Control and Decision Conference (CCDC), Hefei, China, 15–17 August 2022; pp. 3077–3082. https://doi.org/10.1109/ccdc55256.2022.10033970.
20. He, K.; Gao, L.; Han, L.; et al. A Variable-Frequency and Phase-Shifted Based Current Sharing Control for Parallel LLC Resonant Converters with Parameter Differences. In Proceedings of the 2024 27th International Conference on Electrical Machines and Systems (ICEMS), Fukuoka, Japan, 26–29 November 2024.
21. Zhang, S.; Wang, C.; Li, X.; et al. Research on Reduced-Order Model Predictive Control and Parallel Current-Sharing System of LLC Resonant Converters. In Proceedings of the 2026 9th International Conference on Energy, Electrical and Power Engineering (CEEPE), Nanjing, China, 17–19 April 2026; pp. 236–241. https://doi.org/10.1109/ceepe69795.2026.11552125.
22. Cobani, O.; Dimitriuc, C.; Zaman, M.S.; et al. Gradient-Descent Sensorless Current Balancing for Multiphase LLC Converters. In Proceedings of the 2026 IEEE Applied Power Electronics Conference and Exposition (APEC), San Antonio, TX, USA, 22–26 March 2026; pp. 1590–1597. https://doi.org/10.1109/apec51134.2026.11516741.
23. Liu, K.; Xiao, T.; Chen, P.; et al. Virtual-Synchronizer-Based Current Sharing Scheme in m-Phase Resonant DC-DC Converters System. *IEEE Trans. Circuits Syst. II Express Briefs* **2025**, *72*, 853–857. https://doi.org/10.1109/tcsii.2025.3559142.
24. Gao, T.; Sun, G.; Wang, H.; et al. Research on Current Sharing Control Method Based on Duty Cycle Regulation for Interleaved Parallel LLC Resonant Converters. *IEEE J. Emerg. Sel. Top. Power Electron.* **2024**, *12*, 3977–3985. https://doi.org/10.1109/jestpe.2024.3416749.
25. Li, D.; Liu, C.; Wang, L.; et al. Enhanced Dynamic Performance of FSBB Converters Using EPSO-Tuned FOPI Control: From Simulation to Hardware Validation. *IEEE Trans. Power Electron.* **2026**, *41*, 12892–12905. https://doi.org/10.1109/tpel.2026.3665732.
26. Podlubny, I. *Fractional Differential Equations: An Introduction to Fractional Derivatives, Fractional Differential Equations, to Methods of Their Solution and Some of Their Applications*; Academic Press: San Diego, CA, USA, 1998.